Nonreciprocal Phase Shift and Mode Modulation in Dynamic Graphene Waveguides

Chengzhi Qin, Bing Wang, Hua Long, Kai Wang, and Peixiang Lu, *Member, OSA*

***Abstract*—We propose a graphene Ramsey interferometer to study the non-reciprocal phase shift and modulation of surface plasmon polaritons (SPPs). The Ramsey interferometer is constructed by a spatially separated graphene pair that can support two SPP modes. By dynamically modulating the surface conductivity of graphene, the SPP modes will undergo uncompleted cross conversion and an additional phase shift. When adopting two modulation regions in the interferometer, the converted mode will jump back with a nonreciprocal phase shift which can be controlled by the modulation length or phase. The SPP mode of phase shift will interfere with the throughout unconverted one, resulting in arbitrary power arrangement between the two SPP modes. The study may find great applications in plasmonic isolators, phase detectors, and one-way mode converters.**

***Index Terms*—Aharonov–Bohm effect, graphene, phase shift, ramsey interferometer.**

I. Introduction

THE Aharonov–Bohm (AB) effect is a quantum mechanical phenomena in which the electron acquires an additional phase by coupling with the electromagnetic potentials even if both electric and magnetic fields vanish [1]. The AB effect reveals the physical significance of vector potential. Commonly only charged particles can exhibit the AB effect since it arises from the magnetic field. However, recent researches have demonstrated the AB phase and effective gauge field for neutral particles such as photons [2]–[4], phonons [5], [6], and cold atoms [7], [8]. For photons, as proposed by Fang *et al.* in [2] and [3], the photonic AB phase is introduced by controlling the phase of dynamic modulation of refractive index in optical systems. The AB phase corresponds to an effective gauge field for photons, providing a new mechanism to manipulate wave propagation and coupling such as light bending [9], focusing [10], and robust photonic edge states [3], [11].

In a waveguide with dynamic modulation of refractive index, the initial phase of modulation corresponds to a photonic AB phase that can be acquired by the waveguide mode through photonic interband transition [2], [12]. By applying the dynamic modulation to two separated regions in the waveguide, the phase difference of modulation in the two regions can be observed from the mode transmittances of the waveguide. The phase difference corresponds to the gauge-invariant AB phase acquired by light in a close loop, which is associated with an effective gauge field for photons. Since the dynamic modulation can break the time-reversal symmetry, the photonic AB phase is non-reciprocal which can be applied in non-magnetic optical isolators.

In this work, we extend the AB phase to the realm of graphene surface plasmon polaritons (SPPs). Graphene is a two-dimensional material and the manipulation of graphene SPPs will facilitate the development of ultra-compact optical devices [13]–[18]. The AB phase is introduced through indirect interband transition of SPPs in a double-layer graphene waveguide by dynamic modulation of graphene surface conductivity or dielectric permittivity. By cascading two modulation regions with different initial phases, we construct a Ramsey interferometer [19], [20] in which the SPPs can acquire an additional phase shift and exhibit the AB effect. As the indirect transition is unidirectional, the phase shift is non-reciprocal. We also utilize the phase shift to modulate the SPP mode conversion and obtain an arbitrary conversion efficiency. Thanks to the flexible tunability of graphene, the dynamic modulation of surface conductivity can be realized by applying a time-varing gate voltage, which enables high modulation frequency and is compatible for on-chip integration.

II. Band Structure and Indirect Interband Transition

We start by investigating the band structure and indirect interband transition of SPPs in a double-layer graphene Ramsey interferometer. Fig. 1(a) shows a schematic of the interferometer, which consists of two parallel graphene sheets embedded in the dielectrics. The shaded zones denote the two modulation regions of the interferometer separated by the middle unmodulated one. As shown in Fig. 1(b), the waveguide can support the symmetric and anti-symmetric supermodes [21], [22], forming two bands in the band structure. The inserted figures denote the magnetic field distributions of the symmetric and anti-symmetric modes at $\omega_1/2\pi = 30$ THz and $\omega_2/2\pi = 35$ THz, respectively. A photonic interband transition between them can be induced as the dielectric permittivity undergoes a spatial-temporal modulation [23]–[25]

$$\varepsilon(x, z, t) = \varepsilon_d + \delta\varepsilon \cdot \mathrm{sgn}(x) \cdot \cos(\Omega t + qz + \phi). \quad (1)$$

Manuscript received May 19, 2016; revised June 18, 2016; accepted June 29, 2016. Date of publication July 06, 2016; date of current version July 22, 2016. This work was supported in part by the 973 Program under Grant 2014CB921301, in part by the National Natural Science Foundation of China under Grant 11304108, in part by the Natural Science Foundation of Hubei Province under Grant 2015CFA040, and in part by the Specialized Research Fund for the Doctoral Program of Higher Education of China under Grant 20130142120091.

The authors are with School of Physics, Wuhan National Laboratory for Optoelectronics, Huazhong University of Science and Technology, Wuhan 430074, China (e-mail: qinchengzhi@hust.edu.cn; wangbing@hust.edu.cn; longhua@hust.edu.cn; kale_wong@hust.edu.cn; lupeixiang@hust.edu.cn).

P. Lu is also with Laboratory for Optical Information Technology, Wuhan Institute of Technology, Wuhan 430205, China.

Color versions of one or more of the figures in this paper are available online at http://ieeexplore.ieee.org.

Digital Object Identifier 10.1109/JLT.2016.2586959

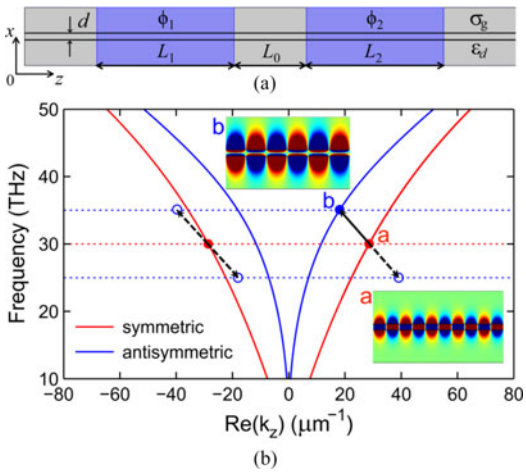

Fig. 1. (a) Schematic of a graphene Ramsey interferometer. The interferometer consists of two parallel graphene sheets embedded in dielectrics with an interlayer space of $d = 50$ nm. The shaded zones denote the two modulation regions with the lengths of L_1, L_2 and initial phases of ϕ_1 and ϕ_2. The length of the middle unmodulated region is $L_0 = 0.5\ \mu$m. Graphene surface conductivity is σ_g and dielectric permittivity is ε_d. (b) Band structure of the double-layer graphene waveguide. The inserted figures marked with a, b illustrate the magnetic field distributions of the symmetric and anti-symmetric supermodes at $\omega_1/2\pi = 30$ THz and $\omega_2/2\pi = 35$ THz, respectively. The solid and dashed arrows denote the allowed and forbidden indirect interband transitions for graphene SPPs in the forward and backward directions.

where $\Omega = \omega_2 - \omega_1$ is the modulation frequency chosen to be resonant with the frequency gap of the two modes. $\delta\varepsilon$, sgn(x), q and ϕ denote the amplitude, transverse profile, wave vector and initial phase of the dynamic modulation, respectively. Note that $k_1 \neq k_2$, the photonic transition here is indirect with $q \neq 0$, which is analogous to the electronic interband transition in indirect band-gap semiconductors [26].

As the transition is indirect, the phase-matching condition should be satisfied. In the forward direction, if we choose $q = k_2 - k_1$ denoted by the solid arrow in Fig. 1(a), the symmetric mode at (ω_1, k_1) can be completely converted to the anti-symmetric one at (ω_2, k_2). The transverse magnetic (TM) polarized electromagnetic field in each dynamic modulated region reads $[\mathbf{E}(x,z,t), \mathbf{H}(x,z,t)] = \sum_m a_m(z)\Psi_m(x)\exp[i(\omega_m t - k_m z)]$ with $a_m(z)$ and $\Psi_m(x) = [\mathbf{E}_m(x), \mathbf{H}_m(x)]$ $(m = 1, 2)$ being the mode amplitudes and transverse profiles. The modes are normalized by $\int_{-\infty}^{+\infty}[E_{x,m}(x)H_{y,m}(x)^* + H_{y,m}(x)E_{x,m}(x)^*]dx = 1$ [27]. Substituting (1) and the field distribution into Maxwell's equations and using rotating wave approximation [2], we can obtain the coupled-mode equations

$$i\frac{d}{dz}\begin{bmatrix} a_1(z) \\ a_2(z) \end{bmatrix} = \begin{bmatrix} 0 & Ce^{-i\phi} \\ C^* e^{i\phi} & 0 \end{bmatrix}\begin{bmatrix} a_1(z) \\ a_2(z) \end{bmatrix}. \tag{2}$$

where $C = 1/2\varepsilon_0(\omega_1\omega_2)^{1/2}\int_{-\infty}^{+\infty}\delta\varepsilon \cdot \mathrm{sgn}(x) \cdot [E_{x,1}(x)E_{x,2}(x)^* + E_{z,1}(x)E_{z,2}(x)^*]dx$, denoting the coupling coefficient between the two modes. The amplitude transfer matrix reads

$$t(z,\phi) = \begin{bmatrix} \cos(|C|z) & -ie^{-i\phi}\sin(|C|z)\dfrac{C}{|C|} \\ -ie^{i\phi}\sin(|C|z)\dfrac{C^*}{|C|} & \cos(|C|z) \end{bmatrix}. \tag{3}$$

The coupling length is given by $L_c = \pi/(2|C|)$, which denotes the distance for complete mode conversion. While in the backward direction under the same modulation, since the phase-matching condition is not satisfied, the interband transition is negligible. Thus the propagation of the incident symmetric mode at $(\omega_1, -k_1)$ is not affected by the dynamic modulation.

The non-reciprocal interband transition of SPPs can also be induced through the dynamic modulation of graphene surface conductivity [28]. In each modulation region, the upper and lower graphene sheets are modulated as $\sigma_{g,1}(z,t) = \sigma_{g,0} + \delta\sigma_{g,0} \cdot \cos(\Omega t + qz + \phi)$ and $\sigma_{g,2}(z,t) = \sigma_{g,0} + \delta\sigma_{g,0} \cdot \cos(\Omega t + qz + \phi + \delta\phi)$, where $\sigma_{g,0}$ and $\delta\sigma_{g,0}$ are the background and modulation amplitude of surface conductivity, respectively. $\delta\phi$ is the phase difference of modulation between the two graphene sheets. As the two supermodes possess opposite symmetries, the coupling between them will occur as $\delta\phi \neq 0$. Here we choose the out-of-phase modulation of $\delta\phi = \pi$ to obtain the maximum coupling strength.

For experimental implementations, the permittivity of the embedded dielectrics can be changed dynamically by applying a periodic electric voltage with a precisely designed *pn-np* diode array [29]. Due to the flexible tunability of graphene [30], [31], the dynamic modulation of graphene surface conductivity can be realized by changing the chemical potential of graphene in the propagation direction through a real-time gate voltage signal. Compared to the dielectric permittivity modulation, the modulation of graphene surface conductivity is preferable since it enables higher modulation frequency and is more compatible for on-chip integration.

III. Nonreciprocal Phase Shift

Now we investigate the effect of the phase of dynamic modulation. As denoted in (1), the perturbation of dielectric permittivity or graphene surface conductivity takes the form of a travelling-wave modulation. When interacting with graphene SPPs, the initial phase of the modulation wave can be added into the SPP mode. According to the coupled-mode equations of (2), the SPP mode picks up a phase of $-\phi$ through an upward interband transition from Ψ_1 to Ψ_2. While for the downward transition from Ψ_2 to Ψ_1, the mode acquires a phase of ϕ. Such an additional phase obtained directly from the external modulation through a mode transition process can be regarded as a photonic AB phase [2], [8]. The phase is a kind of geometric phase [32], which is different from the propagation phase accumulated in the propagation process. Generally, the absolute phase of an optical mode is not detectable since it relies on the choice of time origin. While the effect of phase difference can be detected through an interference setup.

To simulate the AB effect of graphene SPPs, we consider the Ramsey interferometer possesses equal length of modulation region $L_c/2$ and different modulation phases ϕ_1 and ϕ_2. As shown in Fig. 2(a), the symmetric mode Ψ_1 is injected from the left end of the interferometer. The transmission amplitude of Ψ_1 at the right end can be regarded as the interference of Ψ_1 from two pathways. In one pathway, part of Ψ_1 makes an upward transition in the first region and then a downward

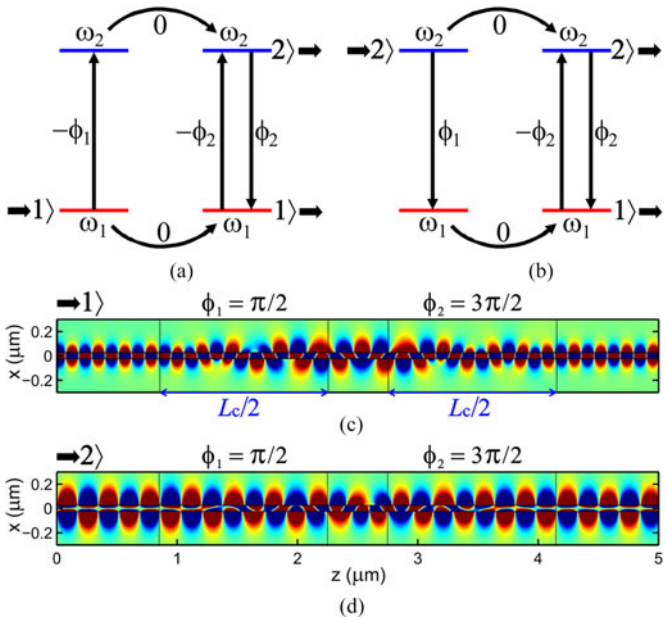

Fig. 2. (a) (b) Schematics of the indirect interband transitions of SPPs in the two modulation regions of the interferometer in the forward direction. ω_1 and ω_2 denotes the frequency of the symmetric and antisymmetric modes marked with $1\rangle$ and $2\rangle$, respectively. ϕ_1, ϕ_2 denotes the additional phase obtained by SPPs through the upward and downward transitions. (c) (d) Simulated SPP mode propagation as the symmetric or antisymmetric mode is incident forwardly under the dynamic modulation of graphene surface conductivity. The initial phases of modulation in the two regions are $\phi_1 = \pi/2$ and $\phi_2 = 3\pi/2$.

transition in the second one, acquiring a total phase shift of $(-\phi_1+\pi/2)+(\phi_2+\pi/2)$. Here only the additional phase shift is considered and the propagation phase is not included. The $\pi/2$ phase shift originates from the mode conversion which is denoted by the factor *i* in the off-diagonal term of the transfer matrix (3). In the other pathway, the remaining unconverted Ψ_1 propagates directly to the right end with an additional phase shift of 0. Thus the phase difference of the two pathways is $\phi_2-\phi_1+\pi$. As the lengths of the modulation regions are both $L_c/2$, the transfer matrix is thus

$$t_n = \frac{\sqrt{2}}{2}\begin{bmatrix} 1 & -ie^{-i\phi_n}C/|C| \\ -ie^{i\phi_n}C^*/|C| & 1 \end{bmatrix}. \tag{4}$$

For the incident symmetric mode Ψ_1, the initial amplitudes are $[a_1(0),0]^T$. After passing through the first modulation region, the mode amplitudes become $[a_1(L_c/2),a_2(L_c/2)]^{\mathrm{T}} = t_1\cdot[a_1(0),0]^T$, which are given by

$$\begin{cases} a_1\left(\dfrac{L_c}{2}\right) = \dfrac{\sqrt{2}}{2}a_1(0) \\ a_2\left(\dfrac{L_c}{2}\right) = \dfrac{-\sqrt{2}}{2}ie^{-i\phi_1}\dfrac{C}{|C|}a_1(0). \end{cases} \tag{5}$$

So we have $|a_1(L_c/2)/a_1(0)|^2 = |a_2(L_c/2)/a_1(0)|^2 = 50\%$, indicating the two parts of symmetric modes from the two pathways have equal amplitudes. The interference of them is thus only determined by the phase difference of the two pathways.

The transmission amplitude of the antisymmetric mode is also the interference of Ψ_2 in two pathways from the interband transition of Ψ_1 in the two regions. And the phase difference of the two pathways is $(\phi_2+\pi/2)-(\phi_1+\pi/2) = \phi_2-\phi_1$. Similarly, if we consider only the antisymmetric mode is incident at the left end shown in Fig. 2(b), the phase difference of the two pathways that contribute to the output Ψ_1 is $\phi_2-\phi_1$. While for the output antisymmetric mode Ψ_2, the phase difference of the two pathways is $\phi_1-\phi_2-\pi$. It shows the mode transmission of the interferometer is uniquely determined by the additional phase shift $\Delta\phi = \phi_2-\phi_1$, which is acquired by the SPPs through the interband transitions. And the phase shift is equal to the phase difference of modulation in the two regions.

More specifically, the phase shift $\Delta\phi$ can be observed from the mode transmittances of the interferometer. We denote T_{ji} as the power ratio of output mode Ψ_j to the incident mode $\Psi_i(i,j=1,2)$. The total transfer matrix of the interferometer is $t = t_2t_1$, so the mode transmittances are $T_{\mathrm{ji}} = |t_{\mathrm{ji}}|^2$, which are given by $T_{11} = T_{22} = [1+\cos(\Delta\phi+\pi)]/2$ and $T_{21} = T_{12} = [1+\cos(\Delta\phi)]/2$. The function of mode transmittances versus the phase shift are known as the Ramsey fringes [12], [33]. The patterns of the fringes obtained here are the same with those of traditional atomic Ramsey interferometers [33]. Since ϕ_1 and ϕ_2 rely on the choice of time origin, they don't correspond to an observable effect. While the phase shift $\Delta\phi$ is observable and can be detected from the mode transmittances. So the phase shift is gauge-invariant and corresponds to the AB phase acquired by SPPs along the closed loop in the interferometer [2], [12]. Note that the phase shift here is non-reciprocal. In the backward direction, due to the existence of large phase mismatch, the indirect interband transition of SPPs can't be induced. Thus the incident mode will not acquire an additional phase shift.

To verify the theoretical analysis, we perform numerical simulations for the SPPs propagation in Figs. 2(c) and (d) by choosing the dynamic modulation of graphene surface conductivity. Here the modulation amplitude is chosen as $\delta\sigma_{g,0} = \sigma_{g,0}/20$ and the coupling length is thus $L_c = 2.8$ μm. The modulation frequency and wavenumber are $\Omega/2\pi = 5$ THz and $q = 10.42$ $\mu\mathrm{m}^{-1}$ with the intial phases being $\phi_1 = \pi/2$ and $\phi_2 = 3\pi/2$. The simulations are performed by using finite element method (FEM) software COMSOL Multiphysics. In the simulation, graphene is modeled as the surface current density boundary condition [34]–[36] that satisfies $\mathbf{n}\times(\mathbf{H}_1-\mathbf{H}_2) = \mathbf{J}_s$, where $\mathbf{H}_{1,2}$ is the magnetic field at the two sides of graphene. The surface current along the parallel direction is given by $\mathbf{J}_s = \sigma_g\cdot E_z$ with E_z the tangential component of electric field. The symmetric and anti-symmetric SPPs modes are excited by launching the transverse mode profiles $H_{y,1}(x)$ and $H_{y,2}(x)$ from the left end of the waveguide. The background graphene surface conductivity $\sigma_{g,0}(\omega,\mu_c,\tau,T)$ is governed by Kubo formula [37], [38], which is determined by the photon frequency ω, chemical potential μ_c, relaxation time τ and temperature T. Here we choose $\varepsilon_d = 2$, $d = 50$ nm, $\mu_c = 0.5$ eV, $\tau = 1$ ps and $T = 300$ K [39]–[41].

Fig. 2(c) shows the magnetic field distributions of SPPs as only the symmetric mode Ψ_1 is injected from the left end of the interferometer. Ψ_1 partly converts to Ψ_2, and return back

to itself at the end of the interferometer. The simulation result agrees well with the theoretical analysis based on the two-path interference. For $\phi_1 = \pi/2$ and $\phi_2 = 3\pi/2$, the phase difference of the two pathways for Ψ_1 is $\phi_2 - \phi_1 + \pi = 2\pi$, leading to a constructive interference for Ψ_1. In contrast for Ψ_2 the phase difference of two pathways is $\phi_2 - \phi_1 = \pi$, resulting in the destructive interference of Ψ_2. So only Ψ_1 exists at the output of the interferometer. The analysis is also applicable for the incidence of antisymmetric mode Ψ_2 shown in Fig. 2(d). For the mode transmittances, we have $T_{11} = T_{22} = 1$ and $T_{21} = T_{12} = 0$, further validating that the incident mode will convert back to itself in the end of the interferometer.

Now we discuss the influence of the loss of graphene on the SPP mode propagation length L. The ohmic loss of graphene is determined by the relaxation time τ [38]. In terahertz and far-infrared ranges, the intraband transition of electrons dominates, the graphene surface conductivity exhibits a Drude-like formula $\sigma_g = ie^2\mu_c/[\pi\hbar^2(\omega + i\tau^{-1})]$ [16] with e, $\hbar$ being the electron charge and reduced Planck constant. The propagation constant of SPPs in a single-layer graphene is $\beta_{sp} = 2i\varepsilon_d k_0/(\sigma_g \eta_0)$ [34], so $L = 1/[2Im(\beta_{sp})] = \tau\mu_c\eta_0 e^2/(4\pi\hbar^2\varepsilon_d k_0)$, which is proportional to τ. Here we choose $\tau = 1.0$ ps which is achievable in experiments [42]. The corresponding propagation length is thus $L = 4.2$ μm. A larger propagation distance of SPPs can be achieved by using high quality graphene with large value of τ.

The loss of graphene doesn't influence the AB interference mechanism associated with the AB phase $\Delta\phi$ and coupling length L_c. $\Delta\phi$ is externally controlled which can't be influenced by the graphene loss. $L_c = \pi/(2|C|)$, C is determined by the transverse mode profiles characterized by the decay constant κ of SPPs. For a single-layer graphene, $\kappa = Re[(\beta_{sp}^2 - \varepsilon_d k_0^2)^{1/2}] = 2\pi\omega\varepsilon_d k_0\hbar^2/(\mu_c\eta_0 e^2)$, which is independent of the relaxation time τ. So the loss of graphene has no influence of the AB effect, thus all the physical results will not change as the loss of graphene varies.

IV. Mode Modulation by the Phase Shift

The non-reciprocal phase shift $\Delta\phi$ provides a new freedom to manipulate wave propagation and coupling. Here we utilize the phase shift to modulate the mode conversion of SPPs. Since the indirect transition of SPPs can only occur in the forward direction, the mode conversion is thus unidirectional. By considering a general interferometer with the lengths of two modulation regions being L_1, L_2 and initial phases ϕ_1, ϕ_2, we have the transfer matrix

$$t_n = \begin{bmatrix} \cos(\theta_n) & -ie^{-i\phi_n}\sin(\theta_n)\dfrac{C}{|C|} \\ -ie^{i\phi_n}\sin(\theta_n)\dfrac{C^*}{|C|} & \cos(\theta_n) \end{bmatrix} \quad (6)$$

where $\theta_n = |C| \cdot L_n$ denotes the modulation strength in each region. For the incident symmetric mode Ψ_1, the transmittances are

$$\begin{aligned} T_{11} = {} & \cos^2(\theta_1)\cos^2(\theta_2) + \sin^2(\theta_1)\sin^2(\theta_2) \\ & - 2\cos(\theta_1)\cos(\theta_2)\sin(\theta_1)\sin(\theta_2)\cos(\Delta\phi) \end{aligned} \quad (7a)$$

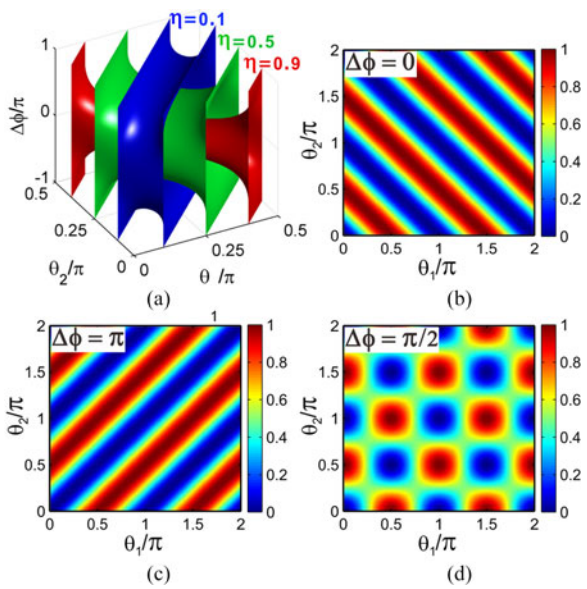

Fig. 3. (a) Contour surfaces of the mode conversion efficiency versus the phase difference $\Delta\phi$ and modulation strengths θ_1 and θ_2 as $\eta = 0.1$, 0.5 and 0.9. (b) (c) (d) The conversion efficiency η as the function of θ_1 and θ_2 for $\Delta\phi = 0$, π, $\pi/2$, respectively.

$$\begin{aligned} T_{21} = {} & \sin^2(\theta_1)\cos^2(\theta_2) + \cos^2(\theta_1)\sin^2(\theta_2) \\ & + 2\cos(\theta_1)\cos(\theta_2)\sin(\theta_1)\sin(\theta_2)\cos(\Delta\phi). \end{aligned} \quad (7b)$$

In principle, both the lengths of the two modulation regions and the modulation phases can be arbitrarily chosen, providing considerable flexibility to control the SPP mode conversion. The conversation efficiency is defined by $\eta(z) = |a_2(z)|^2/|a_1(0)|^2$. At the output end of the interferometer, the conversion efficiency is $\eta = T_{21}$.

Fig. 3(a) denotes the contour surfaces of the conversion efficiency of $\eta = 0.1$, 0.5, and 0.9, respectively. Each contour surface corresponds to a unique output state which is the superposition of Ψ_1 and Ψ_2 with the power ratio of T_{11}/T_{21}. By tuning the phase shift $\Delta\phi$ and modulation strengths in the two regions, one can obtain an arbitrary conversion efficiency from $\eta = 0$ to 100%. The contour surfaces are symmetric with respect to the two planes of $\theta_1 + \theta_2 = \pi/2$ and $\Delta\phi = 0$. As η increases, the length of the surfaces increases and the cross section decreases. Figs. 3(b)–(d) illustrate three horizontal sections in the contour surfaces for $\Delta\phi = 0$, π and $\pi/2$, respectively. When the modulations in the two regions are in phase, that is $\Delta\phi = 0$ shown in Fig. 3(b), the mode transmittances are $T_{11} = \cos^2(\theta_1 + \theta_2)$ and $T_{21} = \sin^2(\theta_1 + \theta_2)$. The mode conversion in the two regions will experience constructive interference. As $\theta_1 + \theta_2 = \pi/2$ (modulo π, same as below), Ψ_1 will convert to Ψ_2 completely after going through the interferometer. In contrast as $\theta_1 + \theta_2 = \pi$, Ψ_1 firstly convert to Ψ_2 and then completely convert back to itself. While for the out-of-phase modulation $\Delta\phi = \pi$ shown in Fig. 3(c), the transmittances are $T_{11} = \cos^2(\theta_1 - \theta_2)$ and $T_{21} = \sin^2(\theta_1 - \theta_2)$, indicating the destructive interference of mode conversion in the two regions. As $|\theta_2 - \theta_1| = \pi/2$, Ψ_1 will convert completely to Ψ_2. While for $|\theta_2 - \theta_1| = \pi$, Ψ_1 partly converts to Ψ_2 in the first region and

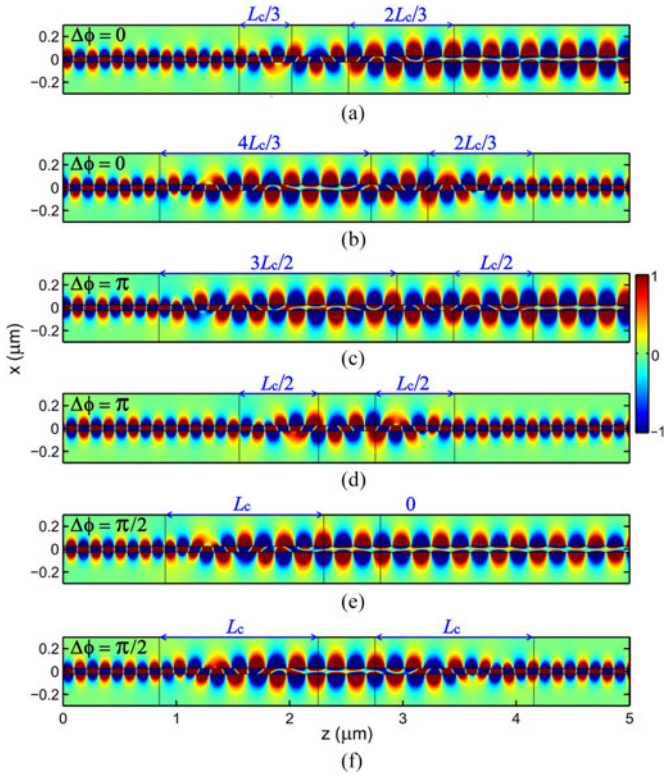

Fig. 4. Magnetic field (H_y) distributions for varied phase shift $\Delta\phi$ and lengths of the two modulation regions L_1 and L_2. The coupling length is fixed as $L_c = 1.4\ \mu$m. (a) $\Delta\phi = 0$, $L_1 = L_c/3$, $L_2 = 2L_c/3$. (b) $\Delta\phi = 0$, $L_1 = 4L_c/3$, $L_2 = 2L_c/3$. (c) $\Delta\phi = \pi$, $L_1 = 3L_c/2$, $L_2 = L_c/2$. (d) $\Delta\phi = \pi$, $L_1 = L_2 = L_c/2$. (e) $\Delta\phi = \pi/2$, $L_1 = L_c$, $L_2 = 0$. (f) $\Delta\phi = \pi/2$, $L_1 = L_2 = L_c$.

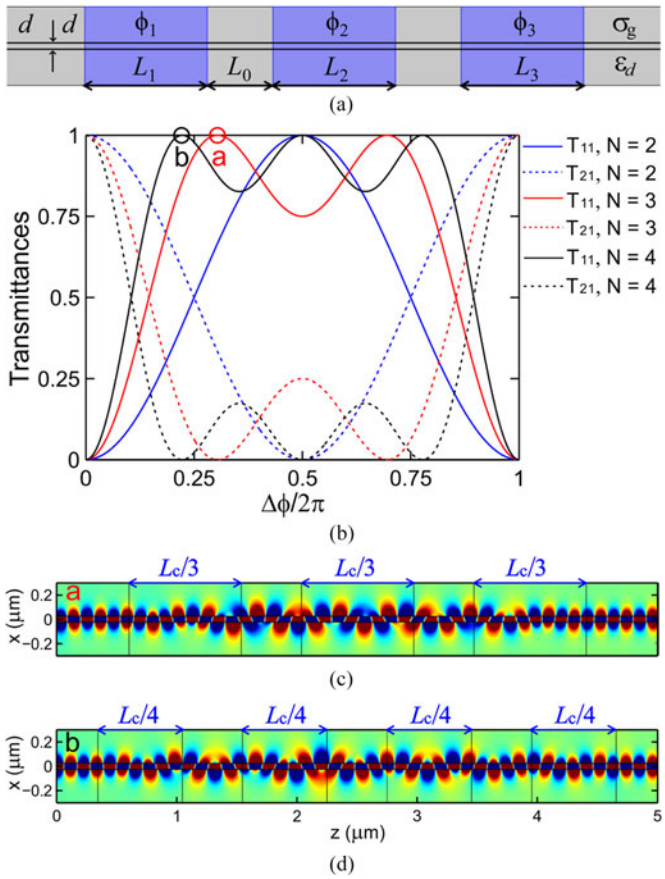

Fig. 5. (a) Schematic of the interferometer with multiple modulation regions. (b) The mode transmittances T_{11} and T_{21} versus the phase difference $\Delta\phi$ of dynamic modulation between adjacent regions as $N = 2$, 3 and 4, respectively. (c) (d) Simulated SPPs propagation in the interferometer for the incident symmetric mode for $N = 3$ and 4. The coupling length is $L_c = 1.4\ \mu$m.

then converts completely back to itself after passing through the second one. For $\Delta\phi = \pi/2$ shown in Fig. 3(d), Ψ_1 will completely convert to Ψ_2 on condition that $\theta_1 = \pi/2, \theta_2 = 0$ (or vice verse). While for the case of $\theta_1 = \theta_2 = 0$ or $\pi/2$, Ψ_1 will ultimately convert back to itself. For other phase difference $0 < \Delta\phi < \pi$ corresponding to a particular horizontal section in the contour surfaces of η, the interferometer can still realize arbitrary power assignment between the two modes at the output end of the waveguide.

To confirm the theoretical analysis, we also perform FEM simulations in Fig. 4 by choosing the dynamic modulation of graphene surface conductivity. The modulation amplitude is chosen as $\delta\sigma_{g,0} = \sigma_{g,0}/10$ and the coupling length is fixed as $L_c = 1.4\ \mu$m. θ_n is thus uniquely determined by the length of modulation region L_n. The length of the unmodulated region is fixed at $L_0 = 0.5\ \mu$m. For the in-phase modulation $\Delta\phi = 0$ shown in Figs. 4(a) and 4(b), the mode conversion accumulates in the two regions, making the output state uniquely determined by the length sum of the two regions. If we fix the length sum and change the length ratio, the output state is unchanged. In Fig. 4(a), the length sum is fixed at L_c with $L_1 = L_c/3$ and $L_2 = 2L_c/3$, Ψ_1 completely converts to Ψ_2. In contrast, the region lengths are $L_1 = 4L_c/3$ and $L_2 = 2L_c/3$ which satisfies $L_1 + L_2 = 2L_c$ shown in Fig. 4(b), Ψ_1 ultimately converts back to itself. While for the out-of-phase modulation $\Delta\phi = \pi$ shown in Figs. 4(c) and (d), the effect of mode conversion cancel each other out in the two regions, making the output state uniquely determined by the length difference of the two regions. In Figs. 4(c) and (d), the length difference is set as $|L_1 - L_2| = L_c$ and 0, the output mode is thus Ψ_2 and Ψ_1, which validates the above analysis in Fig. 3(c). For $\Delta\phi = \pi/2$ showed in Figs. 4(e) and (f) as $L_1 = L_c$, $L_2 = 0$ and $L_1 = L_2 = L_c$, the simulated results can also fairly agree with the analysis in Fig. 3(d).

The Ramsey interferometer with two modulation regions can be extended to that with multiple ones. By engineering the length and phase of modulation in each region, we can control the mode conversion of SPPs more flexibly. As shown in Fig. 5(a), we consider an interferometer with the equal length of modulation region $L_n = L_c/N$ and phase of modulation $\phi_n = \phi_1 + (n-1)\Delta\phi$, $(n = 1, 2, \ldots, N)$, where ϕ_1 is an arbitrary reference phase in the first modulation region with $\Delta\phi$ being the phase difference between neighboring ones. Here we choose $\delta\sigma_{g,0} = \sigma_{g,0}/10$ and the coupling length is thus $L_c = 1.4\ \mu$m. The mode transmittances of the interferometer for $N = 2$, 3, and 4 are shown in Fig. 5(b). The transmittances are symmetric with respect to $\Delta\phi = \pi$ which are independent of the reference phase of ϕ_1. Generally for an interferometer with N modulation regions, there exists $N - 1$ phase shift of $\Delta\phi$ for $T_{11} = 1$. As denoted by the red and black circles in Fig. 5(b), the phase

shift is $\Delta\phi = 0.304\cdot(2\pi)$ and $0.223\cdot(2\pi)$ to reach $T_{11} = 1$ for $N = 3$ and 4, respectively. The corresponding field distributions for the SPPs propagation are shown in Figs. 5(c) and (d). The symmetric mode Ψ_1 incident at the left end experiences partial mode conversion in the interferometer and ultimately return to itself at the right end. The effect for the mode to convert back to itself may find applications in dynamic optical delay lines and buffers. Since the mode conversion efficiency of SPPs can be controlled by engineering the phase of modulation and the length of each region, the interferometer may find applications in one-way mode converters and frequency shifters. Conversely, the phase difference of modulation can be extracted from the mode transmittances, the interferometer with multiple modulation regions may also be applied in phase detectors and phase sensing.

V. Conclusion

In conclusion, we have investigated the AB effect of SPPs in a Ramsey interferometer based on the double-layer graphene waveguide. The AB phase is introduced through the indirect interband transition of SPPs by the dynamic modulation of graphene surface conductivity or dielectric permittivity. As the two modulation regions in the interferometer possess different phases, the SPP modes will acquire a non-reciprocal phase shift and exhibit the AB effect. The phase shift is equal to the phase difference of modulation in the two regions. We also utilize the phase shift to modulate SPP mode conversion and realize arbitrary conversion efficiency. By extending the interferometer of two regions to that with multiple regions, the mode conversion of SPPs can be tuned more flexibly by engineering the phase of modulation and the length of each modulation region. The incident SPP mode can convert back to itself in the multiple region interferometer, which may be applied in dynamic optical delay lines or buffers. As a new mechanism to manipulate wave propagation and coupling, the non-reciprocal phase shift may find wide applications in plasmonic isolators, phase detectors, and one-way mode converters.

References

[1] Y. Aharonov and D. Bohm, "Significance of electromagnetic potentials in the quantum theory," *Phys. Rev.*, vol. 115, no. 3, pp. 485–491, Aug. 1959.

[2] K. Fang, Z. Yu, and S. Fan, "Photonic aharonov-bohm effect based on dynamic modulation," *Phys. Rev. Lett.*, vol. 108, no. 15, Aug. 2012, Art. no. 153901.

[3] K. Fang, Z. Yu, and S. Fan, "Realizing effective magnetic field for photons by controlling the phase of dynamic modulation," *Nat. Photon.*, vol. 6, pp. 782–787, Aug. 2012.

[4] M. Schmidt, S. Kessler, V. Peano, O. Painter, and F. Marquardt, "Optomechanical creation of magnetic fields for photons on a lattice," *Optica*, vol. 2, no. 7, pp. 635–641, Jul. 2015.

[5] D. D Dai and X. Zhu, "An effective gauge potential for nonreciprocal acoustics," *Europhys. Lett.*, vol. 102, no. 1, Apr. 2013, Art. no. 14001.

[6] E. Li, B. J. Eggleton, K. Fang, and S. Fan, "Photonic Aharonov-Bohm effect in photon-phonon interactions," *Nat. Commun.*, vol. 5, Jan. 2014, Art. no. 3225, doi: 10.1038/ncomms4225.

[7] Y. J. Lin, R. L. Compton, K. Jiménez-García, J. V. Porto, and I. B. Spielman, "Synthetic magnetic fields for ultracold neutral atoms," *Nature*, vol. 462, pp. 628–632, Dec. 2009.

[8] J. Dalibard, F. Gerbier, G. Juzeliūnas, and P. Öhberg, "Colloquium: Artificial gauge potentials for neutral atoms," *Rev. Mod. Phys.*, vol. 83, no. 4, pp. 1523–1543, Nov. 2011.

[9] K. Fang, Z. Yu, and S. Fan, "Photonic de Haas-van Alphen effect," *Opt. Express*, vol. 21, no. 15, pp. 18216–18224, Sep. 2015.

[10] K. Fang and S. Fan, "Controlling the flow of light using the inhomogeneous effective gauge field that emerges from dynamic modulation," *Phys. Rev. Lett.*, vol. 111, no. 20, Nov. 2013, Art. no. 203901.

[11] M. Minkov and V. Savona, "Haldane quantum hall effect for light in a dynamically modulated array of resonators," *Optica*, vol. 3, no. 2, pp. 200–206, Feb. 2016.

[12] L. D. Tzuang, K. Fang, P. Nussenzveig, S. Fan, and M. Lipson, "Non-reciprocal phase shift induced by an effective flux for light," *Nature Photon.*, vol. 8, pp. 701–705, Sep. 2014.

[13] A. N. Grigorenko, M. Polini, and K. S. Novoselov, "Graphene plasmonics," *Nature Photon.*, vol. 6, no. 11, pp. 749–758, Oct. 2012.

[14] H. Hu, K. Wang, H. Long, W. Liu, B. Wang, and P. Lu, "Precise determination of the crystallographic orientations in single ZnS nanowires by second-harmonic generation microscopy," *Nano Lett.*, vol. 15, no. 5, pp. 3351–3357, Apr. 2015.

[15] B. Sensale-Rodriguez, "Graphene-based optoelectronics," *J. Lightw. Technol.*, vol. 33, no. 5, pp. 1100–1108, Mar. 2015.

[16] C. Qin, B. Wang, H. Long, K. Wang, and P. Lu, "Bloch mode engineering in graphene modulated periodic waveguides and cavities," *J. Opt. Soc. Amer. B, Opt. Phys.*, vol. 32, no. 8, pp. 1748–1753, Jul. 2015.

[17] Y. Fan, B. Wang, K. Wang, H. Long, and P. Lu, "Talbot effect in weakly coupled monolayer graphene sheet arrays," *Opt. Lett.*, vol. 39, no. 12, pp. 3371–3373, Jun. 2014.

[18] B. Wang, H. Huang, K. Wang, H. Long, and P. Lu, "Plasmonic routing in aperiodic graphene sheet arrays," *Opt. Lett.*, vol. 39, no. 16, pp. 4867–4870, Aug. 2014.

[19] N. F. Ramsey, "A new molecular beam resonance method," *Phys. Rev.*, vol. 76, no. 7, Aug. 1949, Art. no. 996.

[20] N. F. Ramsey, "A molecular beam resonance method with separated oscillating fields," *Phys. Rev.*, vol. 79, no. 6, pp. 695–699, Jul. 1950.

[21] B. Wang, X. Zhang, X. Yuan, and J. Teng, "Optical coupling of surface plasmons between graphene sheets," *Appl. Phys. Lett.*, vol. 100, no. 13, Mar. 2012, Art. no. 13111.

[22] C. Qin, B. Wang, H. Huang, H. Long, K. Wang, and P. Lu, "Low-loss plasmonic supermodes in graphene multi-layers," *Opt. Express*, vol. 22, no. 21, pp. 25324–25332, Oct. 2014.

[23] Z. Yu and S. Fan, "Complete optical isolation created by indirect interband photonic transitions," *Nature Photon.*, vol. 3, no. 11, pp. 91–94, May 2009.

[24] B. Wang, J. Teng, and X. Yuan, "Inelastic scattering of surface plasmon in oscillating metallic waveguides," *Appl. Phys. Lett.*, vol. 98, no. 26, Jun. 2011, Art. no. 263111.

[25] B. Wang, J. Teng, and X. Yuan, "Frequency control of surface plasmons with oscillating metal-insulator-metal waveguides," *Appl. Phys. A*, vol. 107, no. 1, pp. 43–48, Dec. 2011.

[26] B. Amin, I. Ahmad, and M. Maqbool, "Conversion of direct to indirect bandgap and optical response of B substituted InN for novel optical devices applications," *J. Lightw. Technol.*, vol. 28, no. 2, pp. 223–227, Jan. 2010.

[27] K. Okamoto, *Fundamentals and Applications of Optical Waveguides*. San Diego, CA, USA: Academic, 2006, pp. 159–165.

[28] D. Correas-Serrano, J. S. Gomez-Diaz, D. L. Sounas, Y. Hadad, A. Alvarez-Melcon, and A. Alù, "Non-reciprocal graphene devices and antennas based on spatiotemporal modulation," *IEEE Antennas Wireless Propag. Lett.*, vol. 15, pp. 1529–1532, Jun. 2016, doi:10.1109/LAWP.2015.2510818.

[29] H. Lira, Z. Yu, S. Fan, and M. Lipson "Electrically driven nonreciprocity induced by interband photonic transition on a silicon chip," *Phys. Rev. Lett.*, vol. 109, no. 3, Jul. 2012, Art. no. 033901.

[30] A. Vakil and N. Engheta, "Transformation optics using graphene," *Science*, vol. 332, no. 6035, pp. 1291–1294, Jun. 2011.

[31] B. Wang, X. Zhang, F. J. García-Vidal, X. Yuan, and J. Teng, "Strong coupling of surface plasmon polaritons in monolayer graphene sheet arrays," *Phys. Rev. Lett.*, vol. 109, no. 7, Aug. 2012, Art. no. 073901.

[32] L. Lu, J. D. Joannopoulos, and Marin Soljačić, "Topological photonics," *Nature Photon.*, vol. 8, pp. 821–829, Nov. 2014.

[33] J. M. Raimond, M. Brune, and S. Haroche, "Colloquium: Manipulating quantum entanglement with atoms and photons in a cavity," *Rev. Mod. Phys.*, vol. 73, no. 3, pp. 565–582, Jul. 2001.

[34] F. Wang *et al.*, "Rabi oscillations of surface plasmon polaritons in graphene-pair arrays," *Opt. Express*, vol. 23, no. 24, pp. 031136–031143, Nov. 2015.

[35] S. Ke, B. Wang, H. Huang, H. Long, K. Wang, and P. Lu, "Plasmonic absorption enhancement in periodic cross shaped graphene arrays," *Opt. Express*, vol. 23, no. 7, pp. 8888–8900, Apr. 2015.

[36] F. Wang, C. Qin, B. Wang, H. Long, K. Wang, and P. Lu, "Rabi oscillations of plasmonic supermodes in graphene multilayer arrays," *IEEE J. Sel. Topics Quantum Electron.*, to be published, doi: 10.1109/JSTQE.2016.2537205.
[37] A. Vakil and N. Engheta, "Transformation optics using graphene," *Science*, vol. 332, no. 6035, pp. 1291–1294, Jun. 2011.
[38] P. Y. Chen and A. Alù, "Atomically thin surface cloak using graphene monolayers," *ACS Nano*, vol. 5, no. 7, pp. 5855–5863, Jun. 2011.
[39] Y. Fan, B. Wang, K. Wang, H. Huang, H. Long, and P. Lu, "Plasmonic Zitterbewegung in binary graphene sheet array," *Opt. Lett.*, vol. 40, no. 13, pp. 2945–2948, Jul. 2015.
[40] Z. Wang, B. Wang, H. Long, K. Wang, and P. Lu, "Plasmonic lattice solitons in nonlinear graphene sheet arrays," *Opt. Express*, vol. 23, no. 25, pp. 32679–32689, Dec. 2015.
[41] C. Seoánez, F. Guinea, and A. H. Gastro Neto, "Dissipation in graphene and nanotube resonators," *Phys. Rev. B*, vol. 76, no. 12, Sep. 2007, Art. no. 125427.
[42] K. I. Bolotin *et al.*, *Solid State Commun.*, vol. 146, no. 9, pp. 351–355, Mar. 2008.

Chengzhi Qin received the B.S. degree in optics and electronic information from Huazhong University of Science and Technology, Wuhan, China in 2014, where he is currently working toward the Ph.D. degree in physics His research interests include graphene plasmonics and dynamic photonic/acoustic devices.

Bing Wang received the B.S. and the Ph.D. degrees in physics from Wuhan University, Wuhan, China, in 2002 and 2007, respectively. He is currently a Professor of the School of Physics and Wuhan National Laboratory for Optoelectronics, Huazhong University of Science and Technology, Wuhan. His research interests include metal/graphene plasmonics, nanophotonics, nonlinear, and ultrafast optics.

Hua Long received the Ph.D. degree in physics from Huazhong University of Science and Technology, Wuhan, China, in 2008. She is currently an Associate Professor at the School of Physics, Huazhong University of Science and Technology. Her research interests include theoretical and experimental research for interaction of femtosecond laser and materials.

Kai Wang received the Ph.D. degree in physics from Huazhong University of Science and Technology, Wuhan, China, in 2011. He is currently an Associate Professor at the School of Physics, Huazhong University of Science and Technology. His research interests include nanophotonics, nonlinear, and ultrafast optics.

Peixiang Lu received the B.S. degree in physics from Peking University, Beijing, China, in 1987, and the Ph.D. degree from the Shanghai Institute of Optics and Fine Mechanics, Chinese Academy of Sciences, Shanghai, in 1992. He is currently a Professor at the School of Physics and Wuhan National Laboratory for Optoelectronics, Huazhong University of Science and Technology, Wuhan, China. He is a Fellow of the Optical Society of America. His current research interests include ultrafast optics, laser physics, and nanophotonics.